New Journal of Physics
The open-access journal for physics

Stability criteria for a passive electrostatic non-relativistic charged particle storage device

P Hammond[1,4], T J Reddish[2,4], A J Alderman[1], D R Tessier[2] and F H Read[3]

[1] School of Physics, CAMSP, University of Western Australia, Perth, WA 6009, Australia
[2] Department of Physics, University of Windsor, Windsor, N9B 3P4, Canada
[3] Department of Physics and Astronomy, University of Manchester, Manchester M13 9PL, UK
E-mail: hammond@physics.uwa.edu.au and reddish@uwindsor.ca

New Journal of Physics **11** (2009) 043033 (21pp)
Received 2 March 2009
Published 27 April 2009
Online at http://www.njp.org/
doi:10.1088/1367-2630/11/4/043033

Abstract. The general conditions are determined for stable multiple orbits of non-relativistic charged particles in a race-track-shaped optical system. These conditions are then considered in the context of an electrostatic storage ring consisting of two 180° hemispherical deflector analysers connected by two separate sets of cylindrical lenses. The race-track configuration of this type has already been constructed and demonstrated to achieve storage of low-energy (tens of electronvolts) electrons (Tessier *et al* 2007 *Phys. Rev. Lett.* **99** 253201). Incorporating the aberrations of the energy-dispersive electrostatic prisms is found to modify and restrict the general stability conditions. This modified formal matrix theory and the results of charged particle simulations described in this study are in excellent agreement with the observed experimental operating conditions for this electron recycling spectrometer.

[4] Authors to whom any correspondence should be addressed.

Contents

1. Introduction

Circular accelerators and storage rings have a long history, having been used in betatrons, cyclotrons and synchrotrons, and thus the theoretical and experimental issues involving beam stability have evidently been successfully addressed (e.g. [1]–[5]). Virtually all large storage rings are designed for charged particles with relativistic energies and hence use magnetic fields for containment and focusing. Among other factors, this circumvents the problems of electrical breakdown arising from the very high potential differences between adjacent elements within electrostatic accelerators. During the last decade attention has returned to storage rings for non-relativistic charged particles for use in atomic and molecular physics, and devices have been constructed based solely on electrostatic deflectors and lenses [6]. One pioneering system, '*ELISA*' (electrostatic ion storage ring, Aarhus), used two separate 160° sector deflectors, together with four 10° deflectors, to create a race-track-shaped geometry [7, 8]. The straight sections contain four pairs of electrostatic quadrupole lenses (horizontal and vertical focusing) together with an RF system and two regions for experiments. *ELISA* has an overall circumference of ∼7 m with operating energies of typically ∼20–25 keV and has all the advantages associated with the use of electrostatic fields, namely small size, low power consumption (no water cooling), no magnetic hysteresis and the ability to store ions of any mass as electrostatic deflection depends on the kinetic energy and not on the momentum. These features have led to similar electrostatic ion storage systems being designed and constructed (e.g. [9]–[14]).

Recently, Tessier *et al* [15] reported the first results from an innovative, desktop sized electrostatic system for the storage of low-energy (<∼150 eV) electrons, referred to as an electron recycling spectrometer (ERS), in which target gas pressure limited storage lifetimes of ∼50 μs were achieved for ∼30 eV electrons, corresponding to ∼200 orbits of the 0.65 m orbital circumference. The race track design of the ERS, shown schematically in figure 1, consists of two 180° hemispherical deflectors analysers (HDAs) interconnected by two electrostatic lens systems of cylindrical geometry. We deliberately make use of the energy dispersive and focusing properties of HDAs as electrostatic 'prisms' and not merely as devices to 'reflect'

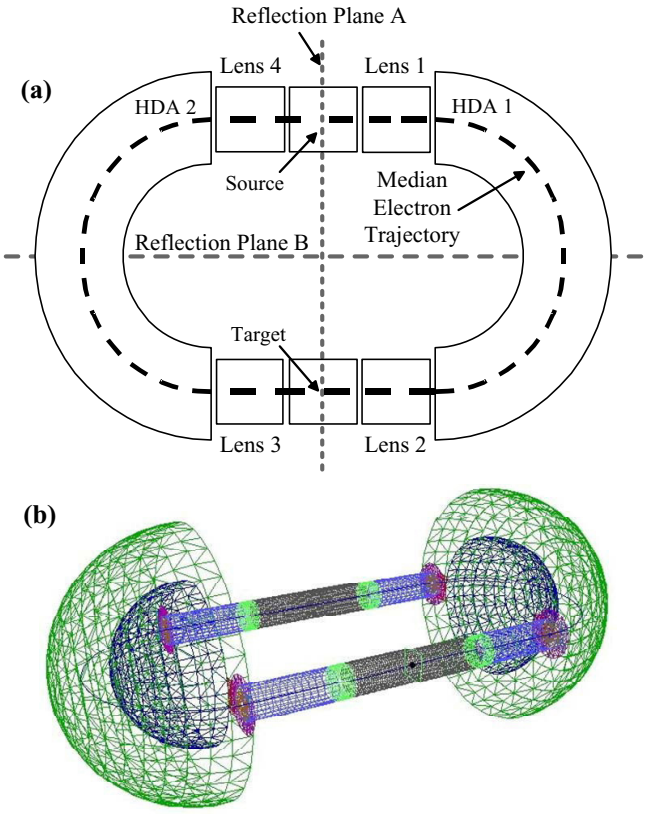

Figure 1. (a) A cross-sectional view of the ERS. The source is at the mid-point of the upper arm, between two lens systems and the target is similarly at the mid-point of the lower arm. The lens systems are connected to HDAs. The reflection planes A and B, discussed in the text, are shown. (b) A three-dimensional view of the ERS as modelled in CPO3D [18].

the trajectory through 180°. Interestingly, conventional HDAs were not used in ELISA, due to their 'strong focusing' properties [7]. Instead, ELISA used 160° sector *hemispherical* electrodes because of their equal focusing in both the 'vertical' and 'horizontal' directions. Later, this was changed to a *cylindrical* geometry [8] to overcome low beam lifetimes resulting from high beam intensities in the narrow beam waists further down the optics [9]. Nevertheless, Tessier *et al* [15] demonstrate that the *ERS*, a passive storage ring with no active feedback components and containing two HDAs, is sufficiently stable against potential loss mechanisms to perform gas-phase experiments. Extensive details of the apparatus will appear elsewhere [16].

The ERS design concept can be adapted to form a recycling system (RS) for any type of charged particle. The prime motivations for developing the ERS were to create (i) a novel source of mono-energetic electrons and (ii) a storage device for positrons and polarized electrons. To move towards these goals it was essential to develop and implement the charged particle optics design principles explored and described in this paper. The practical validity of these principles is demonstrated in the achieved performance of the ERS [15], which can be viewed as a specific example of a generic electrostatic RS for low-energy charged particles.

In section 2, we describe the charged particle optics required for storage in an *RS* using a matrix formalism assuming ideal performance of lenses and HDAs, leading to two

specific operating modes. This formalism is then applied in section 3 to an RS with a specific symmetry in both physical geometry and applied voltages. Specific predicted lens design voltages, obtained using parametrized focal length data from Harting and Read [17], are incorporated into a charged particle trajectory modelling package in which the constructed ERS apparatus is accurately simulated. The effects on stability of incorporating realistic HDA aberration behaviour into the matrix formalism are explored in section 4, leading to energy resolution benefits. Section 5 describes a comparison between the predicted charged particle optics behaviour and experimental results. Overall conclusions are given in section 6.

2. The charged particle optics transfer matrices

In an RS, the charged particle optics design is intended to enable the transport of particles so that they traverse many orbits within the apparatus. The optical design of an RS, which also defines the physical geometry of a system, can be approached in two different ways: (i) through the use of analytical transfer matrices for each optical component and (ii) through the use of a numerical electrostatic charged-particle optics simulation program to integrate the trajectories through large numbers of orbits.

The transfer matrix approach has the advantage of describing the performance of a system in a straightforward mathematical framework that can be extended to predict the performance of an RS for an arbitrary large number of orbits. The disadvantage is the difficulty of including the effects of aberrations. In conventional 'single-pass' systems, aberrations play only a 'one-off' role, whereas in an RS, particles can explore the aberration characteristics extensively since they make multiple passes through the optics. In comparison, the advantage of using a numerical modelling program to track trajectories, such as CPO3D [18], is the implicit inclusion of the effects of aberrations and other non-ideal behaviour. The disadvantage, however, is that accurate modelling requires very large amounts of computer memory and multiple orbits result in very long computational times with the possibility of unavoidable modelling inaccuracies, which may cause cumulative errors and, hence, misleading results.

We have therefore developed a method that makes use of the transfer matrices of the electrostatic elements that are implemented in a numerical model. This predictive approach then allows specific operating settings to be tested in a trajectory integration model through only a few orbits. We shall deal primarily with the first-order properties of the lenses and analysers in the present study, only commenting briefly on third-order aberrations. The third-order aberrations are of course important in practice because they affect the evolution of the effective phase space of the beam, and hence affect the current density and energy resolution, but this restriction does not fundamentally undermine the conditions for orbital stability.

The geometry of the RS considered here is shown in figure 1. In order to make use of symmetry properties in the RS geometry, we consider here the charged particles as originating at the centre of the 'source' region located at the mid-point of the upper arm and travelling in a clockwise direction. Though the ERS [15] actually uses an electron source external to the race-track path[5], these electrons are injected into the mid-point of the upper arm and are then

[5] In an earlier version of the ERS [19], electrons did originate in the source region, but this particular source was abandoned for complex technical reasons. However, with this earlier style of source, one can in principle obtain counter-propagating electron beams circulating around the storage ring, which has the potential for very interesting experiments.

'processed' by the charged particle optics system. We refer to the right-hand HDA in figure 1 as HDA 1, and the left-hand analyser as HDA 2. We shall also refer to the cylindrically symmetric lens, or system of lenses, between the source region and HDA 1 as Lens 1. Similarly, the next lens encountered in the clockwise direction, between HDA 1 and the target region, is Lens 2, followed by Lens 3, HDA 2 and Lens 4, followed by the source region. A feature of this design is that the first-order focusing properties in the vertical and horizontal planes are the same, due to the cylindrical symmetry in the lenses and the radial symmetry in the HDAs. Other important symmetry planes are (i) reflection in the plane bisecting the source and target (plane A in figure 1) and (ii) reflection in the plane bisecting HDA 1 and HDA 2 (plane B in figure 1). We assume, throughout this work, the physical electrode geometry to be symmetric to reflection in planes A and B. In addition, we use the term 'symmetric condition' to describe the voltages applied to the electrodes when they are symmetric to reflection in both planes A and B.

The relationship between the transverse position r_s and slope r'_s, with respect to the (local) optical axis, of a trajectory at the source and the position r_e and slope r'_e of the same trajectory at the entrance to HDA 1 can be expressed by the matrix equation:

$$\begin{pmatrix} r_e \\ r'_e \end{pmatrix} = \begin{pmatrix} a_{00} & a_{01} \\ a_{10} & a_{11} \end{pmatrix} \begin{pmatrix} r_s \\ r'_s \end{pmatrix}, \tag{1}$$

where the quantities a_{ij} are the elements of the transfer matrix m_1 for Lens 1. The forms of the matrix elements a_{ij} depend on the positions of the source and the entrance to HDA 1, the position of the reference plane of Lens 1, the focal lengths f_1 and f_2 and the midfocal lengths F_1 and F_2. It is worth noting that elements a_{00} and a_{11} correspond to the linear and angular magnifications, respectively. Throughout the trajectory mapping procedure we use coordinates of the form r and r' measured with respect to the local coordinate system i.e. those within those elements.

Using the normal conventions within charged particle optics, the transfer matrix for Lens 1 is (e.g. [20]–[22])

$$m_1 = -\frac{1}{f_2} \begin{pmatrix} K_2 & K_1K_2 - f_1f_2 \\ 1 & K_1 \end{pmatrix}, \tag{2}$$

where

$$K_1 = P - F_1, \qquad K_2 = Q - F_2, \tag{3}$$

where P and Q refer to the positions of the source and the entrance to HDA 1, respectively (i.e. they are not necessarily the positions of conjugate objects and images). The relevant lengths are illustrated in figure 2. Note that if Newton's law holds, i.e. if the element $(m_1)_{01}$ is zero, then P and Q correspond to the positions of a conjugate object and image, but this is not generally the case for the present system.

We will consider the *symmetric condition* of operating an RS in which the kinetic energy of the charged particle at the target is the same as that at the source. This is not necessarily a condition that would often be used in practice but is useful to consider before studying the more complex general asymmetric condition to be considered elsewhere. To achieve the symmetric condition, Lenses 1 and 3 are identical, as are Lenses 2 and 4, and if Lenses 1 and 3 are accelerating lenses, then Lenses 2 and 4 are decelerating lenses (and vice versa). Lens 2 has the same geometry and voltages as Lens 1 but is traversed by the charged particles in the

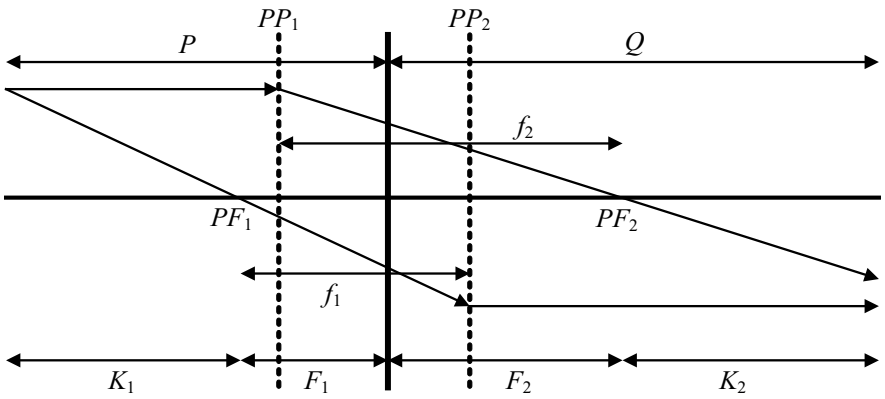

Figure 2. Schematic diagram showing the positions of the principal planes PP_1 and PP_2 and the principal foci PF_1 and PF_2 of an electrostatic lens, together with the focal lengths f_1 and f_2, the mid-focal lengths F_1 and F_2 and the lengths K_1 and K_2 defined in the text. The thick vertical line is the reference plane. The distances P and Q refer here to the positions of the source and the entrance to HDA 1 and do not refer to the positions of a conjugate object and image.

opposite direction to Lens 1 (and similarly for Lenses 3 and 4). Since Lens 2 is effectively a time-reversed version of Lens 1, its transfer matrix is therefore

$$m_2 = -\frac{1}{f_1}\begin{pmatrix} K_1 & K_1K_2 - f_1f_2 \\ 1 & K_2 \end{pmatrix}. \tag{4}$$

The idealized transfer matrices of HDA 1 and HDA 2 are

$$m_{\mathrm{h}} = \begin{pmatrix} -1 & 0 \\ 0 & -1 \end{pmatrix}. \tag{5}$$

This transformation corresponds to the well-known property of 'image inversion' of an HDA. We will address the energy dispersion property of HDAs in section 4.

The overall half-orbit transfer matrix, M_{st}, from the source to the target in the symmetric condition is therefore

$$M_{\mathrm{st}} = m_2 m_{\mathrm{h}} m_1 = \frac{1}{f_1 f_2}\begin{pmatrix} f_1f_2 - 2K_1K_2 & 2K_1(f_1f_2 - K_1K_2) \\ -2K_2 & f_1f_2 - 2K_1K_2 \end{pmatrix}. \tag{6}$$

The optical system from the target to the source is the same as that from the source to the target and so the overall full-orbit transfer matrix, M_{ss}, from the source back to the source is

$$M_{\mathrm{ss}} = M_{\mathrm{st}} M_{\mathrm{st}}. \tag{7}$$

3. Stability criteria for the 'symmetric condition'

The general condition for the stability of an RS [1, 2, 5, 22, 23] is

$$\tfrac{1}{2}|\mathrm{Tr}(M_{\mathrm{ss}})| \leqslant 1. \tag{8}$$

Physically, this signifies that both the overall linear and angular magnifications are not greater than one. If this were not the case, the image size and trajectory angles will become increasingly large with the number of orbits; in other words, the overall combination is that of a diverging lens. This condition can easily be violated unless considerable care is taken, which is the subject of the present study. It should be noted that the equation (8) condition is well known within the circular accelerator physics community (e.g. betatron oscillations) (e.g. [1]–[4]). Therefore we will briefly present the well-established matrix formalism used to describe such oscillations and then consider equations (6)–(8) within this context.

We start by expressing M_{ss} in the usual form, which is analogous to a rotation matrix

$$M_{\mathrm{ss}} = \begin{pmatrix} \cos\theta & L\sin\theta \\ -\dfrac{\sin\theta}{L} & \cos\theta \end{pmatrix} \tag{9}$$

with both θ and L being real quantities, where, for a physically unique solution, $0 \leqslant \theta \leqslant 2\pi$. In this context L is a characteristic length and θ physically corresponds to the angle of rotation of the phase space ellipse for a trajectory traversing one orbit. The elements $(M_{\mathrm{ss}})_{ij}$ in equation (9) can be derived from equations (6) and (7). Note that the form of equation (9) satisfies the trace condition in equation (8). Furthermore, it is well known in charged particle optics that the determinant of the transfer matrix M_{st} must be unity for the symmetric condition, since there is no overall acceleration [5], [20]–[23]. Equation (9) also satisfies this condition, which is an expression of the conservation of phase space (Liouville's theorem) and is also incorporated into the Helmholtz–Lagrange relation.

For a charged particle traversing N orbits the overall transfer matrix M_{ss}^N can be shown to be

$$M_{\mathrm{ss}}^N = \begin{pmatrix} \cos N\theta & L\sin N\theta \\ -\dfrac{\sin N\theta}{L} & \cos N\theta \end{pmatrix}. \tag{10}$$

It should also be noted mathematically that if $|M_{\mathrm{ss}}| \equiv 1$ then the determinant for M_{ss}^N will always be unity, thus satisfying the conservation of phase space for multiple orbits.

The same formalism can be applied not only to the transfer matrix for the complete storage ring, but also to the individual repetitive 'cells', in this case, an combination of two lenses and an HDA, which are repeated to form the closed ring. When the ERS is operated in the symmetric condition, there are two such identical cells, both specified by M_{st} (see equations (6) and (7)). One can therefore show that

$$M_{\mathrm{st}} = \begin{pmatrix} \cos(\theta/2) & L\sin(\theta/2) \\ -\dfrac{\sin(\theta/2)}{L} & \cos(\theta/2) \end{pmatrix}, \tag{11}$$

with, in this case,

$$L^2 = \frac{K_1}{K_2}(f_1 f_2 - K_1 K_2). \tag{12}$$

By considering the element $(M_{\mathrm{st}})_{00}$ in the transfer matrix for half an orbit, then, from equations (6) and (11),

$$(M_{\mathrm{st}})_{00} = \frac{1}{f_1 f_2}(f_1 f_2 - 2K_1 K_2) = 1 - \frac{2K_1 K_2}{f_1 f_2} = \cos(\theta/2). \tag{13}$$

In the limiting cases of $\cos(\theta/2) \to 1, -1$,

$$M_{\mathrm{st}} = \begin{pmatrix} 1 & 0 \\ 0 & 1 \end{pmatrix} \equiv I \tag{14}$$

and

$$M_{\mathrm{st}} = \begin{pmatrix} -1 & 0 \\ 0 & -1 \end{pmatrix} \equiv -I. \tag{15}$$

Physically, equations (14) and (15) result in a non-inverted and 'inverted', i.e. $(r_{\mathrm{s}}, r'_{\mathrm{s}}) \to (-r_{\mathrm{t}}, -r'_{\mathrm{t}})$, image of the source at the target, respectively, the latter requiring two half-orbits to obtain the unit matrix for M_{ss}.

3.1. Type IA and Type IB focusing conditions

The form of M_{st} given by equations (14) can be generally obtained by putting $K_1 = K_2 = 0$ (see equations (6) and (13)), which we will refer to as 'Type IA' focusing. This requires

$$P = F_1, \quad Q = F_2, \tag{16}$$

so that the source is at the first principal focus of the lens and the entrance of HDA 1 is at the second principal focus (see figure 2), which implies that

$$F_1 + F_2 = S, \tag{17}$$

where S is the distance between the source and HDA 1. The condition given by equation (15), which we will refer to as 'Type IB' focusing, requires both (i) $K_1 K_2 = f_1 f_2$ and (ii) K_1 and K_2 being very large and very small lengths, respectively, so that L in equation (12) remains finite.

From the standpoint of the practical use of these focusing conditions, it is essential to establish if they are surrounded by regions of stability or whether they represent isolated stable points in regions of instability. In the following we show that both Type I conditions are of the latter character by examining the form of the matrices as the Type I conditions are approached. Considering the form of L, equation (12) as $\sin(\theta/2) \to 0$ for both conditions, one finds that $L \to 0$ for Type IB and is undefined (0/0) for Type IA, resulting in the leading angular term, $(M_{\mathrm{st}})_{10}$, being ill-defined. For instance, in Type IA focusing, we can represent 'detuning' from equation (14) by introducing the parameters k_1 and k_2, small offsets in P and Q from the equation (16) condition, and setting

$$P = F_1 + k_1, \quad Q = F_2 + k_2 \tag{18}$$

(see also equation (3)). If $k_1 k_2 < 0$ the trace of M_{ss} is greater than 2 and so the system is unstable. On the other hand, if $k_1 k_2 > 0$ the trace is less than 2, but the system is still unstable in the close proximity of the exact Type IA condition, because it can be shown that

$$\theta \approx \pm 4 \left(\frac{k_1 k_2}{f_1 f_2} \right)^{1/2}, \tag{19}$$

$$L \approx \pm \left(\frac{k_1 f_1 f_2}{k_2} \right)^{1/2}. \tag{20}$$

The instability arises from the fact that $(M_{\mathrm{st}})_{01} \propto k_1$, resulting in a rapidly expanding beam size for multiple orbits. Alternatively, $(M_{\mathrm{st}})_{10} \propto k_2$, hence the beam angle will increase rapidly

with N. Similar arguments exist for the Type IB condition. In a real RS, defining apertures aberrations and the finite size of the optical elements will therefore quench these modes of operation. Thus $K_1K_2 \to 0$, f_1f_2 are the so-called 'resonance' conditions to be avoided in the choice of the operating conditions for an RS, and $0 < K_1K_2 < f_1f_2$ gives the limiting values for bounds on $\theta/2$.

3.2. Type II focusing

To explore $\theta/2$ values for $0 < K_1K_2 < f_1f_2$ a further generalization can be made by considering the condition under which a trajectory, after traversing H half-orbits, results in $M_{\mathrm{st}}^H = I$ or $-I$ satisfying, in the half-orbit formulation equivalent of equation (10), the following:

$$\cos(H\theta/2) = 1 - 2\sin^2(H\theta/4) = \pm 1. \tag{21}$$

The ± 1 limits can readily be obtained using the substitution $H\theta/2 = m\pi$, where m is any integer in the range $0 < m < H$. Consequently, a more general condition can be formulated by incorporating $\theta/2 = m\pi/H$ into equation (13) and using the trigonometric identity in equation (21) to obtain

$$\frac{K_1K_2}{f_1f_2} = \sin^2\left(\frac{m\pi}{2H}\right). \tag{22}$$

Equation (22) specifies particular Type II focusing conditions for the RS defined by the values of m and H and which will be referred to as (H,m) modes. The value of m lies in the range $0 < m < H$, which avoids the unstable Type I resonance conditions of $m = 0$ (i.e. $K_1K_2 = 0$) and $m = H$ (i.e. $K_1K_2 = f_1f_2$). When m is an odd integer, the result of H half-orbits is $-I$ and when m is an even integer, the result of H half-orbits is I, the unit matrix. Since only the ratio of m/H appears in equation (22), then $\frac{m}{H} \equiv \frac{nm}{nH}$, where n is any integer and a unique value of $(K_1K_2)/(f_1f_2)$ is produced; i.e., for example the (2,1) mode is physically equivalent to the (4,2) mode. Consequently, although one can more generally regard m as a quasi-continuous variable for large H, there are special (H,m) combinations that are 'irreducible integer fractions'.

In a real RS with a fixed lens geometry (i.e. P and Q), the electrostatic lens properties f_1, f_2, F_1 and F_2 are adjusted with the available voltages. If there are n focusing conditions to satisfy, then there needs to be a minimum of $(n+1)$ independent lens voltages—or n independent lens voltage ratios [17, 24]. In the symmetric condition for the present ERS, each lens is composed of three cylinders at potentials V_1, V_2 and V_3 leading to only two lens parameters that can be varied independently; V_2/V_1 and V_3/V_1. Type II (H,m) focusing (equation (22)) requires only one lens ratio to be varied.

To implement equation (22) and hence determine the design voltages for Type II (H,m) focusing conditions, we have computed the focal lengths of three element cylinder lenses as a function of V_2/V_1 for a given V_3/V_1 using the parameterization coefficients determined by Harting and Read [17] for their calculated focal lengths. In the range of voltage ratios used here, the parameterized focal lengths agree by better than 1% with Harting and Read's calculated focal lengths, which themselves were estimated to have an absolute uncertainty better than 1%. As an example of the design voltage approach, we consider the case of $V_3/V_1 = 2$ with $V_1 = 18$ V (as used for the experimental data presented in section 5). Figure 3 shows $(K_1K_2)/(f_1f_2)$ and $\mathrm{Tr}(M_{\mathrm{ss}})/2$ (see equation (8)) as a function of V_2. Two regions of predicted stability arise from equation (22) under these conditions; one region is narrow in V_2 and centred around 4 V and the second region is broad in V_2 and spans ~85–160 V.

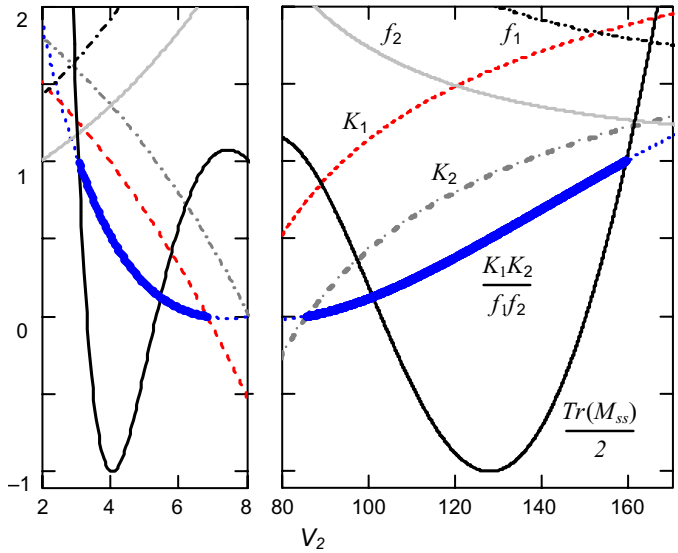

Figure 3. Plots of characteristic lens parameters as a function of V_2, as derived from the parameterizations given by Harting and Read [17] for $V_3/V_1 = 2.0$ and for $P = 2.7D$, $Q = 2.75D$, where D is the lens diameter. K_1 and K_2 are only physically meaningful in this context if they are positive quantities. K_1K_2/f_1f_2 is of relevance to the (H,m) modes through equation (22). For example, when this ratio equals 0.5, $(H,m) = (2,1)$ and $[\mathrm{Tr}(M_{ss})]/2$ is -1. Stability requires $[\mathrm{Tr}(M_{ss})]/2$ to be between ± 1 (equation (8)). Two regions of stability, set by V_2, are therefore predicted: a narrow region between ~3.1 and 6.8 V and a broad region between ~86 and 159.4 V.

We now consider examples of particular focusing conditions. In the case where $H = 2$ and $m = 1$, equation (22) is simply

$$\text{Type II (2, 1)} \qquad \frac{K_1K_2}{f_1f_2} = \sin^2\left(\frac{\pi}{4}\right) = \frac{1}{2} \tag{23}$$

and the trajectories only retrace their paths after two complete orbits. This Type II (2,1) focusing condition can be achieved by giving M_{st} the form (see equations (11) and (12))

$$\text{Type II (2, 1)} \qquad M_{st} = \begin{pmatrix} 0 & K_1 \\ \frac{-1}{K_1} & 0 \end{pmatrix}. \tag{24}$$

In the case where $H = 3$, there are two possible integer m values ($m = 1, 2$) giving the following focusing conditions:

$$\text{Type II (3, 1)} \qquad \frac{K_1K_2}{f_1f_2} = \sin^2\left(\frac{\pi}{6}\right) = \frac{1}{4}, \tag{25}$$

$$\text{Type II (3, 2)} \qquad \frac{K_1K_2}{f_1f_2} = \sin^2\left(\frac{2\pi}{6}\right) = \frac{3}{4}. \tag{26}$$

Thus after $1\frac{1}{2}$ orbits one can achieve either $-I$ ($m = 1$) or I ($m = 2$), the former requiring three full orbits to return to the path of the original trajectory. Both modes are stable (in the absence of aberrations—see section 4) as $L \neq 0$ or ∞.

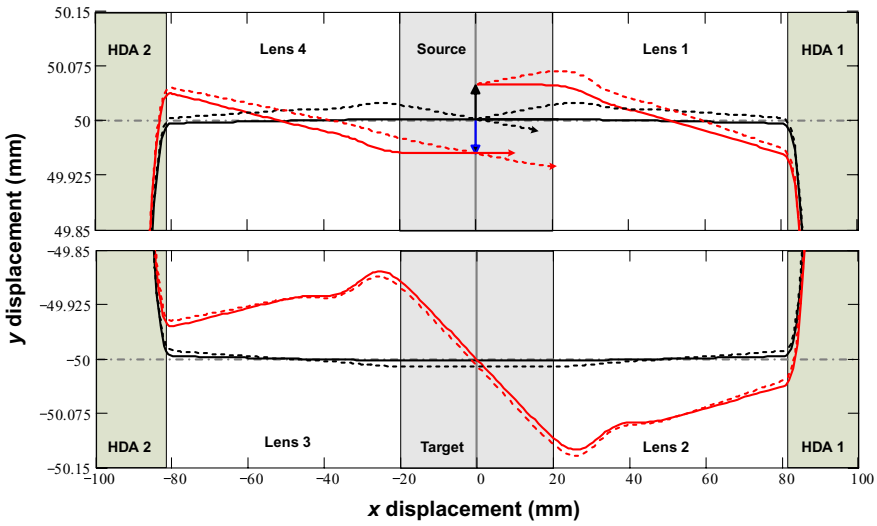

Figure 4. A set of four trajectories obtained using CPO3D program for the ERS when the Type II (2,1) focusing condition is satisfied (equation (23)). Note the significant differences in the x and y scales, which distorts the elliptical trajectories in the HDAs. Trajectories originating from two $(0, y)$ positions in the 'source' region, each with two different launch angles, traverse the ERS in the clockwise direction for just over one orbit. The 'image' in the 'target' region after half an orbit is a 'transform' of the initial object. As characterized by the Type II (2,1) mode, the image at the source after one orbit of the ERS is an inverted form of the initial object, and after two complete orbits the charged particles will retrace their trajectories.

The consistency of the predicted performance of the RS between the matrix-based model and the trajectory integration model can be explored by selecting particular (H,m) combinations, which give, through equation (22), specific values for $(K_1K_2)/(f_1f_2)$. These then lead, through figure 3, to specific predicted V_2 voltages. Figure 4 shows the results of the procedure applied to the Type II (2,1) focusing condition specified by equations (23) and (24). Here a set of four paraxial trajectories, modelled in CPO3D using the figure 3 design voltage for $(K_1K_2)/(f_1f_2) = 1/2$, are tracked through one orbit and shown in the source and target lens stacks. The trajectories start in the source region and traverse the ERS in the clockwise direction. One observes that after one full orbit the image at the source is inverted in both position and angle. After two complete orbits, therefore, the final trajectories would overlay on the initial trajectories i.e. the image would, in the absence of aberrations, coincide with the initial object. In the target region the four trajectories form a 'transform' of the source region object. The radial extent is small since $(M_{\mathrm{st}})_{00} = 0$ (equation (24)), whereas the target angles are proportional to the initial off-axis object position by means of $(M_{\mathrm{st}})_{10}$.

In the target region, small trajectory angles result from starting trajectories in the source region near the optical axis, as shown in figure 5. It can also be seen in figure 5 that as the source angle is increased the non-paraxial behaviour of the system of lenses and HDA is increasingly probed, resulting in trajectories in the target region that do not exactly follow Type II (2,1) focusing as indicated by the increasingly nonzero angles as a function of r_{t} of the trajectories

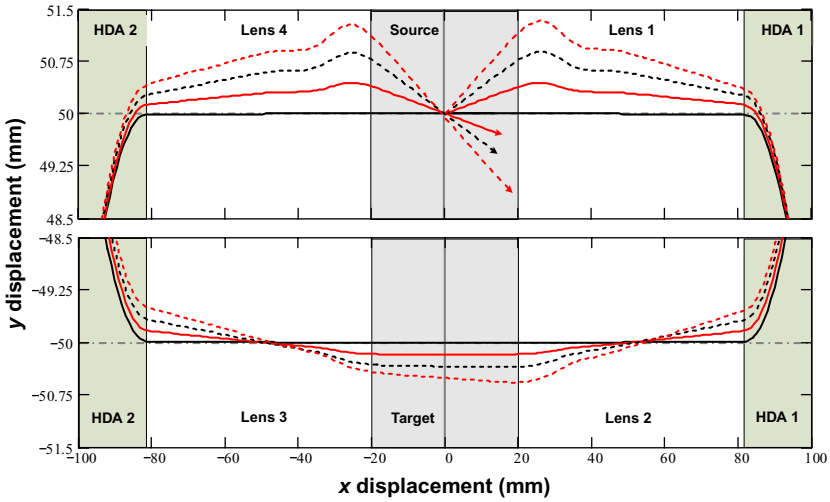

Figure 5. A set of four trajectories obtained using CPO3D program for the ERS when the Type II (2,1) focusing condition, as in figure 4. Trajectories in the target region showing the transform of a source object that lies on the optical axis but having a wide range of initial angles. Note that the trajectories for the largest initial angles show signs of aberrations, as the trajectories lack symmetry in the target region.

in the target. Analysis of these trajectories shows that as rays become increasingly non-paraxial there is a small increase in the value of $\theta/2$ by which they are described.

Though the non-paraxial trajectories in figure 5 do not necessarily follow the Type II (2,1) behaviour expected for paraxial rays, they do lead to an overall time averaged stable 'beam' envelope when tracked through many orbits, as shown in figure 6. Here one of the trajectories showing non-paraxial behaviour from figure 5 has been tracked through 37 orbits and fails, through small differences in both r and r', to return to itself after two orbits. Consequently, it represents a Type II orbit for which both H and m are very large but lead to a value of $(m\pi/2H)$ in equation (22) that is close to the Type II (2,1) value of $(\pi/4)$ from equation (23).

In general, even for paraxial trajectories, the angle $(m\pi/2H)$ is quasi-continuous and arises from the ratio of integers m/H, where both H and m can become very large. In such circumstances stability can still be readily achieved with the trajectory retracing itself after a very large number of orbits and having a 'beam' envelope similar to that shown in figure 6. Thus, in stark contrast to the two Type I focusing conditions, the Type II (H,m) modes described by equation (22) are embedded in a sea of stability (in the absence of aberrations). This is very important in practice, as it is unreasonable to expect to achieve in a real apparatus exact small integer values for both m and H either because of aberrations (including fringing fields at the HDA entrances and exits) leading to non-paraxial behaviour and imperfect voltage tuning (deliberate detuning or insufficient precision, i.e. noise and ripple) leading to non-exact setting of m and H.

Though the stability conditions presented in this section have been developed in the context of electrostatic lenses and HDAs, they also apply to any other system (e.g. magnetic lenses) which can be described in thick lens formalism and in which an equivalent device to an HDA is available.

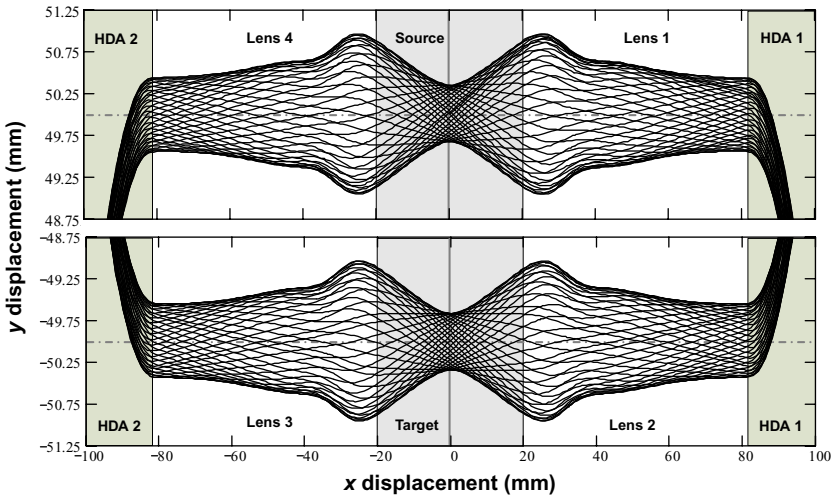

Figure 6. Multiple orbits of a trajectory when the lens parameters approximately satisfy the Type II (2,1) focusing condition (equation (23)).

4. HDA: the consequences of non-ideal behaviour

In the preceding discussion we have assumed each HDA to operate as an idealized device with a transport matrix given by equation (5). Of course this ideal cannot be achieved in practice and necessitates a more complex description of the trajectory within the HDA. There are many studies (e.g. [25]–[27]) exploring the exact analytical expressions that give the HDA exit position r_f and angles r'_f of a trajectory as a function of entry position r_e from the median radius R_0 of the HDA, angle r'_e and energy $E = E_0 + \Delta E_0$, where $|\Delta E_0| \ll E_0$ for an HDA of pass energy E_0. For convenience, and with no loss of generality, since we are primarily concerned with stability issues in this study, we will adopt the well-known simple approximations for the effect of different entrance coordinates on the exit position (e.g. [25, 28]) which apply to HDAs with ideal field terminations at the entrance and exit planes. Moreover, we will continue this discussion within the symmetric condition, adopting the same pass energies for both HDAs. The transformation of the position and slope of a trajectory as the particle traverses HDA 1 is then given by

$$\begin{pmatrix} r_f \\ r'_f \end{pmatrix} = m_h \begin{pmatrix} r_e \\ r'_e \end{pmatrix} + \begin{pmatrix} \Delta r(r_e, r'_e, \Delta E_0) \\ \Delta\varphi(r_e, r'_e, \Delta E_0) \end{pmatrix}, \tag{27}$$

where Δr and $\Delta\varphi$ are the radial and angular offsets introduced through a single traverse through an HDA and may, in general, each be related to the entrance coordinates r_e, r'_e and ΔE_0. These 'translated' electrons then traverse Lens 2 and arrive at the target. Hence, after one half-orbit, the trajectory coordinates r_t and r'_t in the target region are given by

$$\begin{pmatrix} r_t \\ r'_t \end{pmatrix} = M_{st} \begin{pmatrix} r_s \\ r'_s \end{pmatrix} + m_2 \begin{pmatrix} \Delta r\left(r_e, r'_e, \Delta E_0\right) \\ \Delta\varphi\left(r_e, r'_e, \Delta E_0\right) \end{pmatrix}. \tag{28}$$

In situations in which neither Δr nor $\Delta\varphi$ depends on the HDA entrance coordinates r_e and r'_e, then after h half-orbits the position r_h and slope r'_h of a trajectory at the source (even h) or

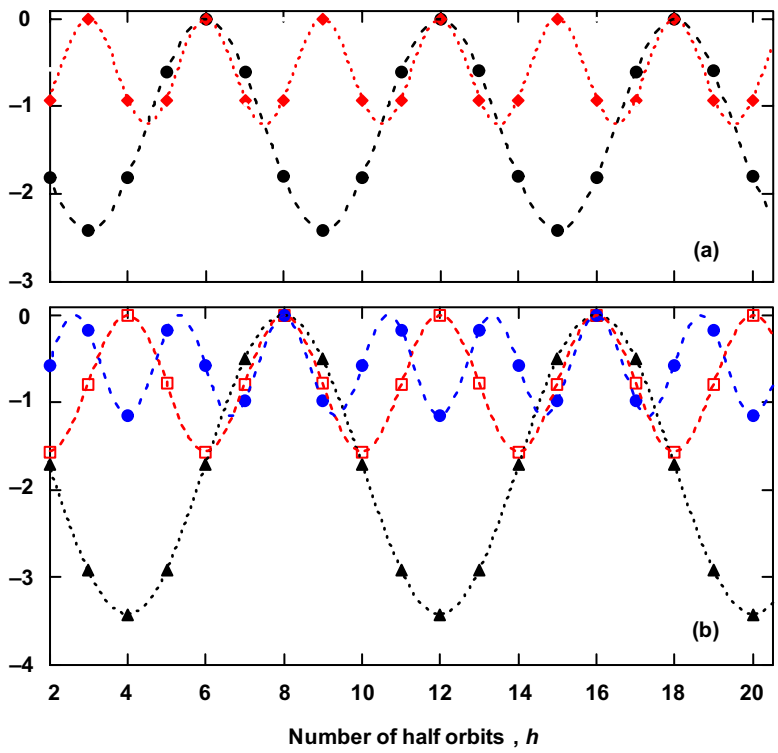

Figure 7. $(Sm_2)_{00}$ for the (H,m) modes as a function of half-orbit number h: (a) ●- - -● (3,1) and ◆···◆ (3,2); (b) ▲····▲ (4,1), □- - -□ (2,1) and ●- - -● (4,3).

target (odd h) are given by

$$\begin{pmatrix} r_h \\ r'_h \end{pmatrix} = M_{\mathrm{st}}^h \begin{pmatrix} r_{\mathrm{s}} \\ r'_{\mathrm{s}} \end{pmatrix} + Sm_2 \begin{pmatrix} \Delta r(\Delta E_0) \\ \Delta\varphi(\Delta E_0 \end{pmatrix}, \tag{29}$$

where

$$S = I + M_{\mathrm{st}} + M_{\mathrm{st}}^2 + M_{\mathrm{st}}^3 + \ldots + M_{\mathrm{st}}^{h-1}. \tag{30}$$

Analysis of the matrices M_{st}^h and Sm_2 (equation (29)) for each (H,m) combination reveals that they are cyclical in h with a cycle period of $2H/m$ half-orbits. In general, all matrix elements of both M_{st}^h and Sm_2 are zero when $h = 2nH$, where n is an integer. The individual matrix elements within M_{st}^h and Sm_2 each oscillate as a function of h between bounding values that vary slowly with m/H.

Figure 7 shows the values of $(Sm_2)_{00}$ for the (3,1), (3,2), (4,1), (2,1) [≡(4,2)] and (4,3) modes as a function of the number of half-orbits, h. The form of $(Sm_2)_{11}$ is similar to that of $(Sm_2)_{00}$, as a function of h, with both having a maximum value of zero, whereas $(Sm_2)_{01}$ and $(Sm_2)_{10}$ oscillate around a value of zero. All elements of M_{st}^h oscillate around a value of zero. Consider, as examples of general behaviour trends, the $(Sm_2)_{00}$ values in figure 7 for each of the (H,m) modes shown. It can been seen that the leading terms $(Sm_2)_{00}$ and $(Sm_2)_{11}$ in radial and/or angular aberrations are increasingly negative for half a cycle, and decreasingly negative for the other half of the cycle. The cross-terms $(Sm_2)_{01}$ and $(Sm_2)_{01}$ (not shown in figure 7) result in aberrations that increase from zero for a quarter of a cycle, and decrease to zero for the other quarter. The overall behaviour is dominated by the leading terms involving $(Sm_2)_{00}$

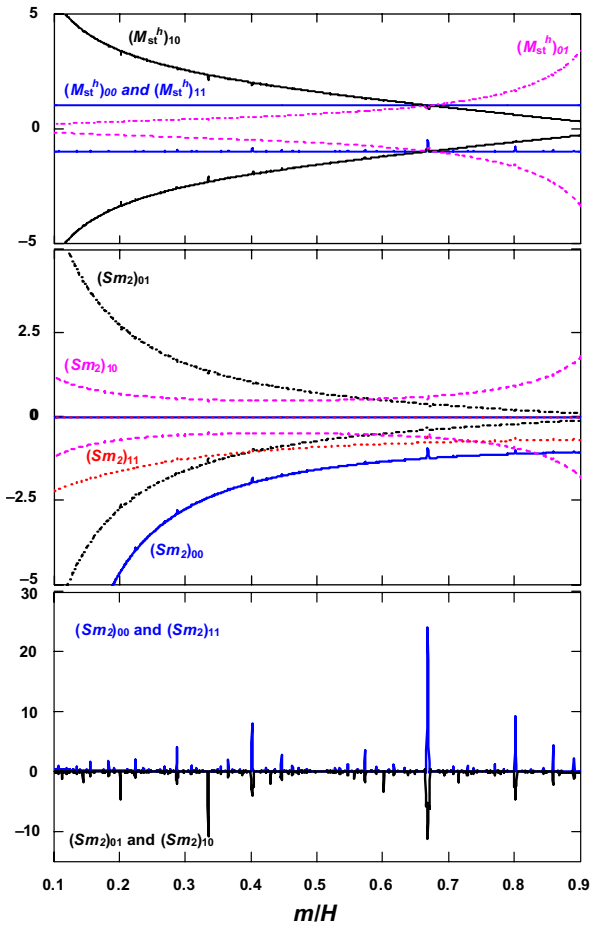

Figure 8. The $M^h_{\rm st}$ and Sm_2 matrices as a function of m/H for 120 half-orbits: (a) bounding values of the $M^h_{\rm st}$ matrix elements, (b) bounding values of the Sm_2 matrix elements and (c) the fine structure decreases of the Sm_2 matrix element bounding values presented as a percentage of the overall bounding value trend (NB: the $(Sm_2)_{00}$ and $(Sm_2)_{11}$ curve has been inverted for clarity of presentation).

and $(Sm_2)_{11}$, with the result that though trajectories can be lost on apertures during increasing portions of a cycle, there is no net 'accumulation' of aberration components over many cycles.

The bounding values of the matrix elements of both $M^h_{\rm st}$ and Sm_2 as a function of m/H for $h = 120$ are shown in figures 8(a) and (b). The fine details of fluctuations from the Sm_2 bounding values are shown in figure 8(c). Inspection of figure 8(c) reveals a small reduction in the bounding values of most matrix elements near the locations of (H,m) modes predominately, but not exclusively, with odd H and even m. These fluctuations decrease in magnitude and width as h increases. Consideration of all of the $M^h_{\rm st}$ and Sm_2 matrix elements as a function of m/H, and using figures 7 and 8 as a guide, suggests that the modes most susceptible to trajectory loss on apertures are those with m/H values approaching 0 and 1. In these regions many matrix elements are larger than in the central m/H region around 0.5, leading to trajectories with larger spreads in r and r' than in the central region. The consequence of these effects in the source

and target regions is that trajectories tend to form 'beams' at low m/H over a wide region of space but with near zero angles, while at high m/H, beams tend to have wide angular ranges emanating from small regions of space. This behaviour is to be expected when approaching the Type I focusing conditions.

4.1. An energy filtering focusing condition

Using the well-known first-order approximation for the HDA energy dispersive properties results in an explicit version of equation (27)

$$\begin{pmatrix} r_{\mathrm{f}} \\ r'_{\mathrm{f}} \end{pmatrix} = m_{\mathrm{h}} \begin{pmatrix} r_{\mathrm{e}} \\ r'_{\mathrm{e}} \end{pmatrix} + \begin{pmatrix} 2R_0 \Delta E_0 / E_0 \\ 0 \end{pmatrix}. \tag{31}$$

For a given ΔE_0, the shift in position, Δr, depends only on the HDA geometry, R_0, and pass energy, E_0. Since the aberration Δr is independent of r_{e} and r'_{e}, it can be considered in the context of equation (29). (Note that while the physical geometries of the two HDAs in the ERS are identical, their operational pass energies need not be [15], but this asymmetric operating condition will not be considered here.)

For the symmetric Type II (2,1) mode it can be shown that for N full-orbits, for odd N,

$$\begin{pmatrix} r_{\mathrm{sf}}^{(N)} \\ r_{\mathrm{sf}}^{\prime(N)} \end{pmatrix} = \begin{pmatrix} -r_{\mathrm{si}} - \dfrac{4K_1 R_0}{f_1} \dfrac{\Delta E_0}{E_0} \\ -r'_{\mathrm{si}} \end{pmatrix}, \tag{32}$$

and for even N,

$$\begin{pmatrix} r_{\mathrm{sf}}^{(N)} \\ r_{\mathrm{sf}}^{\prime(N)} \end{pmatrix} = \begin{pmatrix} r_{\mathrm{si}} \\ r'_{\mathrm{si}} \end{pmatrix}. \tag{33}$$

The radial divergences described by equation (32) correlate with the minima shown in figure 7(b) for the (2,1) mode and are caused by the energy difference ΔE_0 from the nominal pass energy of the HDA. Since they are proportional to ΔE_0, apertures can be used at appropriate positions to restrict the energy range of the instrument. The Type II (2,1) mode is therefore suitable for energy analysis. The energy resolution is simply given by the resolving capability of *one* orbit, as the trajectories retrace after two orbits. Examining (H,m) modes more generally, as shown in figures 7 and 8, we deduce that all modes achieve the form of equation (33) since Sm_2 repetitively takes values of zero. Between these zeros, a sinusoidal variation in the value of Δr occurs the amplitude of which increases with decreasing values of m/H. This behaviour has the effect that modes with lower m/H values are energy filtered more effectively than modes of higher m/H. Thus, within this energy aberration approximation, higher m/H modes are likely to dominate the storage pattern since less charged particles are filtered in collisions with apertures. Importantly, the energy resolution is stable with h after one cycle of $2nH$ half-orbits is complete, in the absence of the effects of higher order aberration terms and any mechanical misalignment. We therefore have in the RS the potential for a stable, energy-resolved storage ring for charged particles of 'switchable' energy resolution, where the switching can be achieved by selecting appropriately different m/H regions by the choice of V_2 (see figure 3). Further numerical studies using CPO3D (see figures 4–6), which implicitly includes aberrations, could be used to explore this topic further, since it is likely that the effects of apertures and higher order aberrations will further improve the energy resolving capability of the ERS.

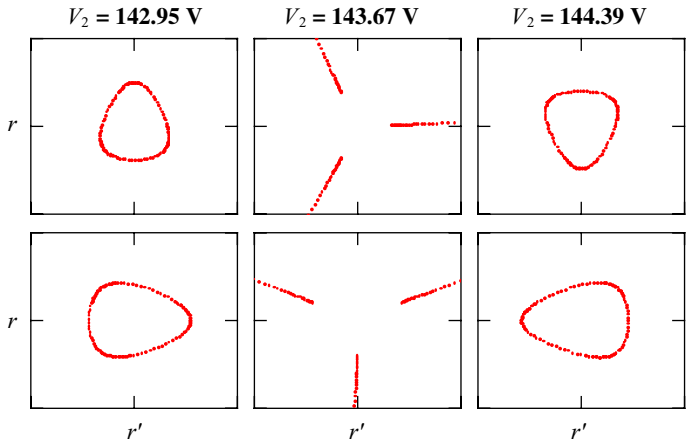

Figure 9. Trajectory coordinates (r, r') in the source/target (upper row) and at the HDA entrances (lower row) for three V_2 voltages in the vicinity of the (3,2) focusing condition with $V_1 = 18$ V and $V_3 = 36$ V (see section 5): left column, 0.72 V below; centre column, at the voltage; and right column, 0.72 V above.

4.2. HDA angular aberrations in the orbital plane: mode loss

The next aberration of highest order is the angular aberration of the HDAs in the orbital plane, where at the median energy E_0 the radial position at the exit of an HDA decreases by $2R_0 r_{e^2}'^2$. The transformation of the position and slope of a trajectory by an HDA is then given by

$$\begin{pmatrix} r_f \\ r_f' \end{pmatrix} = m_h \begin{pmatrix} r_e \\ r_e' \end{pmatrix} + \begin{pmatrix} -2R_0 r_e'^2 \\ 0 \end{pmatrix}. \tag{34}$$

This matrix is of the same form as equation (27), although the translation now depends on the initial angle r_e' with the result that equation (29) does not apply. To explore the consequences of equation (34) in a matrix approach an iterative numerical calculation has to be performed in which the HDA entry coordinates are determined for each half-orbit. Using this approach we find that the (3,2) mode becomes unstable, with trajectories at the source and the target increasing slowly in both r and r'. This instability is shown in the phase space diagram of figure 9 for values of V_2 in the close vicinity of the predicted V_2 location of the (3,2) mode. At the (3,2) mode location the trajectory is unstable and diverges. Either side of this location the proximity of the (3,2) mode shows up through the production of a distorted 'triangular-shaped' phase space. In the trajectory integration model, similar unstable behaviour is observed for the (3,2) mode though the triangular shape of phase space extends over a V_2 range approximately 10 times wider than computed from the numerical implementation of equation (34). To a lesser extent, similar behaviour occurs for the (5,2) mode. The behaviour of these two modes within these two computational approaches is markedly different from the observed behaviour of other modes explored. It suggests that the angular aberration of the HDA described by equation (34) is responsible for mode loss for at least these two even m modes; it is not unlikely that such angular aberrations make all odd H, even m modes unstable (see experimental results in section 5). The trajectory integration results suggest that the influence of these modes in phase space is more extensive than equation (34) predicts, implying that the strength of the angular aberration is underestimated by this approximation.

4.3. Other aberrations

We now consider the HDA aberrations in the plane orthogonal to the 'orbital'—or energy dispersive—plane. Equation (5) is still the appropriate expression for the idealized focusing, and the discussion and analysis in section 3 are valid for both planes. Trajectory integration calculations in the non-orbital plane have identified a similar set of (H',m') focusing conditions to those observed in the orbital plane, which also exhibit cyclic half-orbit periods of $2n'H'$. Modes specified by m'/H' are located at V_2 values ~10 V higher than their orbital plane counterparts of the same m/H.

In contrast to the (H,m) modes in the orbital plane, all of the (H',m') modes examined have displayed stability. The different V_2 locations of the same modes are likely to arise from non-ideal HDA transfer matrices and different forms of aberrations between the orbital and non-orbital planes. Only weak coupling between the two planes has been observed in the modelling, in accordance with the theoretical coupling expressions given by Wollnik [29].

Finally, we note that the lenses connecting the HDAs have both angular and chromatic aberrations. These aberrations are likely to be only important when trajectories are non-paraxial though more significant for larger angles in the source and target regions, such as in the high m/H region, but of lesser effect than the HDA angular and chromatic aberrations. Non-paraxial trajectories occur more readily when an RS is operated in the region of low V_2, which in the current ERS is about 4 V. In the stability region set by high V_2 values, the lower end of this region tends to generate trajectories over a large range of r_t with a range of smaller angles r_t', whereas in contrast the upper end of this region tends to generate trajectories from a small range of small r_t with a large range of larger r_t'. This latter group of trajectories is likely to be more affected by angular aberrations in the lenses.

5. Experimental results

The storage of electrons as a function of time and voltage V_2 for $V_3/V_1 = 2.0$ is shown in figure 10, with a logarithmic shading scale for electron yield. (Similar trends are also observed for $V_3/V_1 = 1.0$ and 3.5 [30].) Long-term electron storage is observed over specific ranges of V_2, namely ~4, ~98–102, ~106–114 and ~124–136 V. The figure also shows the V_2 values for selected modes arising from equation (22) with focal lengths computed from the parameterizations of Harting and Read [17] and resulting in the $(K_1K_2)/(f_1f_2)$ values shown in figure 3. There is excellent agreement between the predicted V_2 voltages for the (2,1) and (3,1) modes and observed bands of electron storage. There is a loss of storage in the vicinity of the predicted voltage for the (5,2) mode. The predicted voltages for the (4,1) and (7,2) modes also correlate with the observed structure if predicted voltages are reduced by ~3% in value. Table 1 gives observed V_2 voltages for various modes and compares these with theoretical predictions arising from equation (22) using the parameterized focal lengths and the V_2 locations of (H,m) modes in the trajectory integration model.

The reduction in intensity of the observed yield bands in the vicinity of the (2,1), (3,1) and (4,1) modes may be indicative of improving the energy resolving capabilities as a function of decreasing m/H, as proposed in section 4. The experimental results also lend support to the suggestion of mode loss in the region of the (5,2) and (7,2) odd-H, even-m modes proposed to arise from HDA orbital plane angular aberrations. However, the observed regions of instability are very much broader in V_2 than the matrix formalism would suggest.

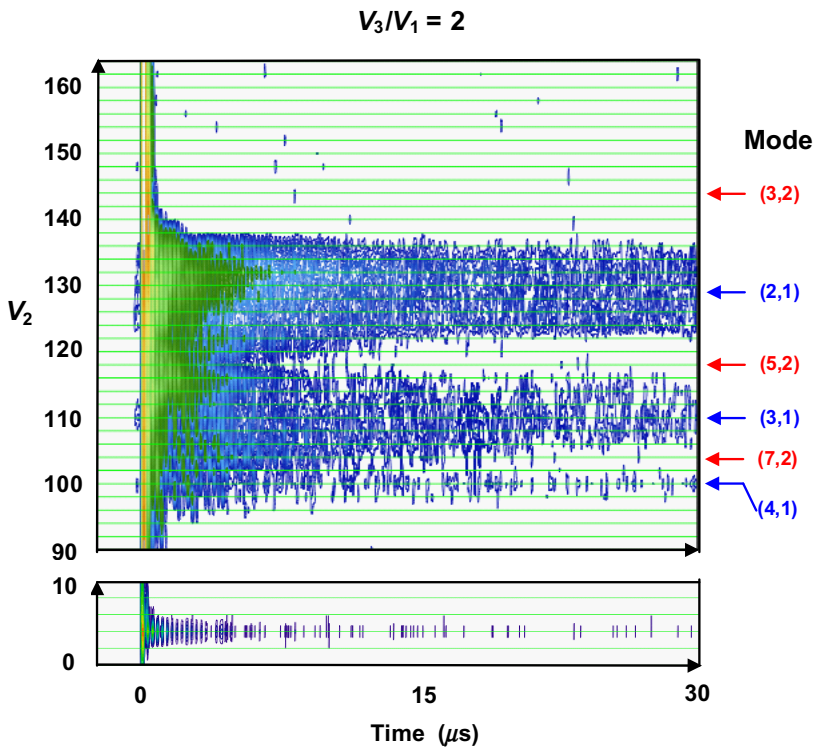

Figure 10. Mosaic contour plot of the logarithm of the ERS yield as a function of V_2 (in 2 V intervals) showing several regions of stability, the most intense being at $V_2 \approx 130$ V for these operating conditions ($V_3 = 36$ V and $V_1 = 18$ V). No further stable conditions were found outside of this V_2 range. Each peak corresponds to the initial electron pulse performing additional orbits, with a period of $\sim$260 ns, around the ERS. The decay in the yield is due to a variety of factors, including residual gas scattering, and is discussed further in [15].

A striking discrepancy between the theoretical description and the experimental results is the non-observation of storage for V_2 voltages above $\sim$136 V. Though the computational results predict the (3,2) mode to be unstable it seems unlikely that the influence of this mode causes the observed behaviour.

In the ERS used in the present studies, the HDAs were field terminated with correctors geometrically very similar to those introduced by Jost [31], since their design is straightforward to mechanically implement accurately. Even then they do not produce the perfect field termination assumed in the development of aberration expressions. Our trajectory integration model included Jost correctors and would be expected to be a reasonable representation of the actual ERS. In the constructed system the middle element of each of the three element cylinder lenses was split into two equal sized cylinders, with the voltage of each cylinder differing by at most 10%, which allowed for compensation of small mechanical tolerance and misalignments in the manufactured components. Lateral imperfections in mechanical alignment of the optical elements, however, would be very difficult to compensate by small changes in the operating voltages. Although the ERS was designed and constructed with a high degree of precision alignment, such imperfections could have a profound effect on performance, as they would

Table 1. The predicted V_2 values for a series of (H,m) modes using the matrix formalism and the parametrized focal lengths with those found using the trajectory integration model using [18]. There is excellent agreement between both approaches and the experimentally observed modes shown in figure 10.

(H,m) mode	K_1K_2/f_1f_2 (from equation (22))	Predicted type	V_2 lens voltage (V)		
			Observed[a]	From equation (22) using parameterized focal lengths from [17]	Trajectory integration model[b]
(2,1)	0.500	Stable	∼128	128.0	128.0
(3,1)	0.250	Stable	∼110	111.1	110.2
(4,1)	0.147	Stable	∼100	103.0	101.3
(4,3)	0.854	Stable	No yield	150.2	151.2
(5,3)	0.654	Stable	No yield	137.7	137.9
(7,2)	0.188	Unstable	∼104	106.4	105.2
(5,2)	0.345	Unstable	∼118	117.8	117.4
(3,2)	0.750	Unstable	No yield	143.7	144.1

[a]Data recorded in 2 V steps.
[b]Trajectory integration voltages that produce half-orbit periods of $2H/m$ to within 1%. The voltage for the (3,2) mode is difficult to determine because instability produces rapid increases in both r and r' (see figure 9).

result in non-colinear optical axes between the lens elements in the source lens stack and target lens stacks and angular misalignments between the lens stacks and the two HDAs.

6. Conclusions

This theoretical study has investigated the overall transfer matrix in a non-relativistic electrostatic charged particle storage ring consisting of two HDAs and four lenses, under symmetrical operating conditions. The connection between the characteristic cardinal lengths of 'thick' lenses and idealized HDAs and the stability condition for 'circular' accelerators has been explicitly established. We have identified a general stability condition for this electrostatic storage ring, which will be invaluable for understanding the operation and performance of the ERS and in the future design of similar electrostatic systems. These general stability conditions also apply to any other system to which thick lens formalism can be applied and in which an equivalent device to an HDA described by the same simple transfer matrix is available. In the electrostatic system, the effects of energy dispersion and angular aberrations in real HDAs have been considered. We demonstrate that though these important terms affect the phase space of the recycling beam, they do not detrimentally undermine the overall principle of stability, but do introduce regions of inherent instability. Excellent agreement is achieved between theoretical predictions and observed behaviour in an apparatus constructed following the design principles described here. This analytical study builds on foundations already established in the high energy (circular accelerator) community. Yet its fresh insights—particularly when considering the energy dispersive properties of HDAs—will be both of practical relevance and aid future theoretical studies.

Acknowledgments

We thank the Paul Instrument Fund, administered by the Royal Society, and the Australian Research Council for financial support of this work. TJR acknowledges the Canadian funding agencies CFI, OIT and NSERC, together with the University of Windsor, for financial support. Preliminary computational studies of an early ERS lens format by Peter J Harvey at the University of Manchester and discussions with Dr Ben G Birdsey are also acknowledged.

References

[1] Persico E, Ferrari E and Segre S E 1968 *Principles of Particle Accelerators* (New York: Benjamin)
[2] Rosenblatt J 1968 *Particle Acceleration* (London: Methuen)
[3] Krinsky S, Perlman M L and Watson R E 1983 *Handbook on Synchrotron Radiation* vol 1 ed E E Kock (Amsterdam: North-Holland) p 65
[4] Duke P J 2000 *Synchrotron Radiation: Production and Properties* (Oxford: Oxford University Press)
[5] Lawson J D 1977 *The Physics of Charged Particle Beams* (Oxford: Oxford University Press)
[6] Andersen L H, Hebner O and Zajfman D 2004 *J. Phys. B: At. Mol. Opt. Phys.* **37** R57
[7] Møller S P 1997 *Nucl. Instrum. Methods* A **394** 281
[8] Møller S P and Pedersen U V 2001 *Phys. Scr.* **T92** 105
[9] Tanabe T, Chida K, Noda K and Wantanabe I 2002 *Nucl. Instrum. Methods* A **482** 595
[10] Welsch C P, Schempp A and Schmidt-Böcking H 2003 *Hyperfine Interact.* **146** 253
[11] Welsch C P *et al* 2004 *Phys. Rev. ST Accel. Beams* **7** 080101
[12] Tanabe T, Chida K and Noda K 2002 *Nucl. Instrum. Methods* A **482** 595
[13] Jinno S, Takao T, Hanada K, Goto M, Okuno K, Tanuma H, Azuma T and Shiromaru H 2007 *Nucl. Instrum. Methods* A **572** 568
[14] Danared H *et al* 2006 *AIP Conf. Proc.* **821** 465
[15] Tessier D R, Niu Y, Seccombe D P, Reddish T J, Alderman A J, Birdsey B G, Read F H and Hammond P 2007 *Phys. Rev. Lett.* **99** 253201
[16] Niu Y, Tessier D R, Sullivan M R, Seccombe D P, Thorn P A, Reddish T J, Alderman A J, Birdsey B G, Read F H and Hammond P 2009 in preparation
[17] Harting E and Read F H 1976 *Electrostatic Lenses* (Amsterdam: Elsevier)
[18] CPO Programs online at http://www.electronoptics.com/
[19] Tessier D R, Niu Y, Seccombe D P, Reddish T J, Alderman A J, Birdsey B G, Hammond P and Read F H 2006 *Australian IOP Congress Proceedings* vol 50 ed R Sang and J Dobson (Parkville, VIC: Australian IOP) ISBN 0-9598064-7-4, WC0328
[20] Moore J H, Davis C C and Coplan M A 1989 *Building Scientific Apparatus* 2nd edn (Reading, MA: Perseus)
[21] Hawkes P W and Kasper E 1989 *Principles of Electron Optics* (New York: Academic)
[22] Wollnik H 1987 *Optics of Charged Particles* (Orlando: Academic)
[23] Courant E D and Snyder H S 1958 *Ann. Phys.* **3** 1
[24] Martinez G, Sancho M and Read F H 1983 *J. Phys. E: Sci. Instrum.* **16** 631
[25] Hadjarab F and Erskine J L 1985 *J. Electron Spectrosc. Relat. Phenom.* **36** 227
[26] Caprari R S 1995 *Meas. Sci. Technol.* **6** 1063
[27] Zouros T J M and Benis E P 2002 *J. Electron Spectrosc. Relat. Phenom.* **125** 221
[28] Kuyatt C E and Simpson J A 1967 *Rev. Sci. Instrum.* **38** 103
[29] Wollnik H 1967 *Focusing of Charged Particles* vol 2 ed A Septier (New York: Academic) 163
[30] Tessier D R 2008 The development of an electrostatic storage ring for low energy electrons *PhD Thesis* University of Windsor, Canada
[31] Jost K 1979 *J. Phys. E: Sci. Instrum.* **12** 1001